Measurement of Monolayer Viscosity Using Noncontact Microrheology

Roie Shlomovitz, Arthur A. Evans, Thomas Boatwright, Michael Dennin, and Alex J. Levine

Phys. Rev. Lett. **110**, 137802 — Published 25 March 2013

DOI: 10.1103/PhysRevLett.110.137802

Measurement of monolayer viscosity using non-contact microrheology

Roie Shlomovitz,[1] Arthur A. Evans,[1] Thomas Boatwright,[2] Michael Dennin,[2] and Alex J. Levine[1, 3]

[1]*Department of Chemistry & Biochemistry UCLA, Los Angeles, CA 90095-1596*
[2]*Department of Physics & Astronomy UCI, Irvine, CA 92697*
[3]*Department of Physics & Astronomy, UCLA, Los Angeles, CA 90095-1596*

(Dated: February 27, 2013)

Microrheological studies of phospholipid monolayers, bilayers, and other Langmuir monolayer systems are traditionally performed by observing the thermal fluctuations of tracers attached to the membrane or interface. Measurements of this type obtain surface moduli that are orders of magnitude different than those obtained using macroscopic or active techniques. These large discrepancies can result from uncertainties in the tracer's coupling to the monolayer or the local disruption of the monolayer by the tracer. To avoid such problems, we perform a microrheological experiment with the tracer particle placed at a known depth beneath the monolayer; this avoids the issues mentioned at the cost of generating a weaker, purely hydrodynamic, coupling between the tracer and the monolayer. We calculate the appropriate response functions for this submerged particle microrheology and demonstrate the technique on three model monolayer systems.

PACS numbers: 68.18.-g,87.16.dm,47.55.N-,83.85.Cg

Langmuir monolayers, formed by surfactants at an air-water interface, have long served as a testing ground for exploring broken symmetry phases in low dimensional systems [1, 2]. They also serve as a model for biological membranes: a lipid monolayer in a Langmuir trough allows for precise chemical control and experimental access to a mimic of one leaflet of a cell membrane [3–6]. In both cases, rheological probes can provide essential data on the low energy excitations of such complex phases and their moduli, as well as measurements of relevance to biomechanics at the cellular level [7]. These rheological measurements, however, have proven to be problematic. Two main approaches have been employed: macrorheology using, for example, oscillatory rheometers, or driven needles or disks floating in the monolayer [8–11], and microrheology in which the thermal (Brownian) motion of particles in the monolayer are tracked [12–14]. The former has difficulties measuring very fragile or compliant surface phases, and may, due to the macroscopic deformations imposed, access the nonlinear response regime. In light of these difficulties, the latter microrheological approach seems promising, but currently suffers from a "missing modulus" problem: when both macro- and microrheological approaches are compared, the microrheological data reports moduli up to four orders of magnitude lower [15].

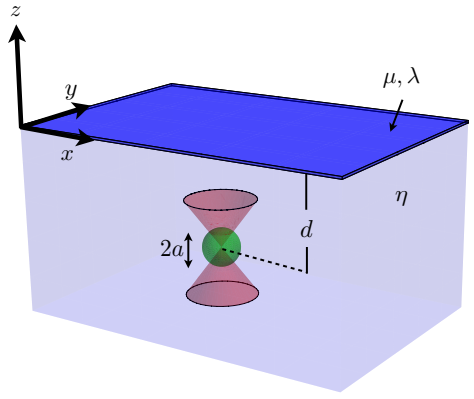

FIG. 1: Schematic diagram for non-contact monolayer and membrane microrheology. The tracer particle of radius a is submerged a depth d beneath the monolayer/membrane, and its fluctuation spectrum is measured using the optical trap.

Two potential causes for these large discrepancies are the uncertainty in tracer positioning and the poorly understood boundary conditions between the particle and the monolayer. The interpretation of the particle tracking microrheology is based on the assumption that the tracer is embedded in the monolayer [16, 17], but this is hard to guarantee since it is difficult to resolve the vertical position of the tracer with sub-micron precision; moreover, higher surface pressures or more elastic monolayers may drive the tracer into the subphase. Even if the particle is embedded in the monolayer, its presence may locally disrupt the monolayer's structure – an effect seen in three dimensional microrheology [18] necessitating more difficult two-particle [19, 20] approaches. Even without such disruptions, the dynamics of the three phase contact line on the particle generates more complex dynamics, which have not been generally accounted for [21].

In this Letter we demonstrate a non-contact approach to membrane and interfacial microrheology, where we use the measurement of the fluctuations of submerged tracers as a function of their depth to infer the viscoelastic properties of the monolayer above them. At the expense of a weaker and purely hydrodynamic coupling between the tracer and the monolayer, we eliminate the issues associated with the direct interaction of the tracer

and the fragile monolayer. We present the calculation of the submerged particle response function necessary to relate the fluctuation data to the interfacial modulus, and apply this microrheological technique to three monolayers: dipalmitoylphophatidylcholine (DPPC), arachidic acid (AA), and eicosanol. We obtain results consistent with previous measurements.

We begin by calculating the velocity response function for a spherical particle of radius a in a fluid with viscosity η, submerged a depth d beneath a monolayer (see Fig. 1). We choose a coordinate system such that the fluid is of infinite lateral extent and depth (in the $-z$ direction), and bounded by the monolayer interface at $z = 0$. The particle oscillates at a frequency ω. At the relevant frequencies (< 100kHz) we may neglect fluid inertia and use the Stokes equations for the fluid velocity field $\boldsymbol{v}$ [22]:

$$\nabla p - \eta\nabla^2\boldsymbol{v} = \boldsymbol{f} \quad (1)$$
$$\nabla\cdot\boldsymbol{v} = 0, \quad (2)$$

where p is the hydrostatic pressure that enforces the fluid incompressibility and $\boldsymbol{f} = \boldsymbol{F}e^{-i\omega t}\delta(z+d)\delta(\boldsymbol{x}_\perp)$ is the applied oscillatory point force representing the probe, with $\boldsymbol{x}_\perp = (x, y)$ the lateral position vector. To study the fluctuations of the tracer in the plane parallel to the monolayer, we set $\boldsymbol{F} \parallel \hat{x}$. A more general solution for any force distribution can be found by superposition [23], but is unnecessary here. Given the surface tension τ of the systems of interest and the amplitude A of particle motion, the relevant capillary number $Ca = \eta A\omega/\tau \sim 10^{-6}$, so we may also neglect the vertical deflection of the interface. These corrections are generally small, see Ref. [23] and supplemental materials.

The fluid velocity vanishes far from the point of force application, and, in the absence of height undulations, we require that the fluid velocity $v_z = 0$ at the interface. There, we also impose a no-slip condition relating the displacement field of the viscoelastic monolayer $\boldsymbol{u}$ to the fluid velocity $\boldsymbol{v}$; in the frequency domain this implies that $v_\alpha|_{z=0} = -i\omega u_\alpha$, where Greek indices run over the coordinates x and y only. Stress balance in the interfacial monolayer requires [24]

$$\mu\partial^2 u_\alpha + (\mu+\lambda)\partial_\alpha\partial_\beta u_\beta + \frac{1}{2}\eta\left(\partial_\alpha v_z + \partial_z v_\alpha\right)\Big|_{z=0} = 0, \quad (3)$$

where the Lamé constants λ, μ must be interpreted as complex, frequency-dependent quantities. The first two terms correspond to the stresses induced by strain (and strain rate) in the monolayer, which must balance the hydrodynamic stresses from the subphase in the third term. $\lambda \to \infty$ corresponds to an incompressible monolayer.

We solve Eqs. (1),(2), and (3) subject to the no-slip boundary condition in order to determine the velocity amplitude of the tracer sphere $\boldsymbol{V}$ in response to the applied force. Using the linearity of the Stokes equations, we divide the solution into two parts, i.e. $\boldsymbol{v} = \boldsymbol{v}^{(1)} + \boldsymbol{v}^{(2)}$. The first part $\boldsymbol{v}^{(1)}$ is the flow field resulting from a point force at the position of the probe, but with the monolayer replaced by a *perfect* slip surface; this field satisfies the force balance in the bulk, but does not satisfy the the stress balance condition on the monolayer. To correct this, we add the second solution $\boldsymbol{v}^{(2)}$, which is the fluid velocity field induced by the negative of the unbalanced surface stresses from $\boldsymbol{v}^{(1)}$ and satisfying the homogeneous equations, Eqs. (1), (2), i.e., with $\boldsymbol{f} = 0$. The physical solution, $\boldsymbol{v}^{(1)} + \boldsymbol{v}^{(2)}$, now satisfies all the necessary stress balance conditions in the bulk and in the interface. Associated with each bulk velocity field $\boldsymbol{v}^{(1,2)}$ there is an in-plane membrane displacement $\boldsymbol{u}^{(1,2)}$ determined by the no-slip matching condition, and from which the interfacial displacement field can be computed.

The perfect slip solution $\boldsymbol{v}^{(1)}$ can be obtained using an "image solution" in analogy to electrostatics (see, for example, [22, 25, 26]) resulting in a combination of flows due to the point force and its reflection about the $z = 0$ plane. This yields the hydrodynamic response of the subphase to the applied point force assuming that the interface at $z = 0$ can exert no shear stresses. The perfect slip solution in the spatial Fourier domain is

$$v_j^{(1)} = \frac{F_x}{\eta k^2}\left(\delta_{xj} - \hat{k}_x\hat{k}_j\right)\cos(k_z d) \quad (4)$$
$$u_\beta^{(1)} = \frac{F_x}{2\eta\omega i}e^{-k_\perp d}\left[\frac{-2\delta_{x\beta}}{k_\perp} + \frac{k_x k_\beta}{k_\perp^3}(1 + k_\perp d)\right], \quad (5)$$

where $\boldsymbol{k}$ and $\boldsymbol{k}_\perp$ are the three- and two-dimensional (in the plane of the interface) wavevectors respectively. By symmetry, the normal velocity $v_z^{(1)}$ vanishes at the surface ($z = 0$), so that the associated normal displacement is zero, $u_z^{(1)} = 0$. Projecting the in-plane components of the interfacial velocity into longitudinal and transverse channels, $u_\beta = u_\beta^{(L)} + u_\beta^{(T)}$, we find

$$u_\beta^{(L1)} = \mathcal{L}_{\beta\alpha}u_\alpha^{(1)} = -\frac{F_\alpha}{2\eta\omega i}e^{-k_\perp d}\left(\frac{k_\alpha k_\beta}{k_\perp^3}(1 - k_\perp d)\right) \quad (6)$$
$$u_\beta^{(T1)} = \mathcal{T}_{\beta\alpha}u_\alpha^{(1)} = -\frac{F_\alpha}{\eta\omega i}e^{-k_\perp d}\left(\frac{\delta_{\alpha\beta}}{k_\perp} - \frac{k_\alpha k_\beta}{k_\perp^3}\right), \quad (7)$$

using the the two-dimensional longitudinal and transverse projection operators $\mathcal{L}_{\alpha\beta} = k_\alpha k_\beta/k_\perp^2$ and $\mathcal{T}_{\alpha\beta} = \delta_{\alpha\beta} - \mathcal{L}_{\alpha\beta}$. From Eq. (3) and noting that the fluid stresses on the interface due to $\boldsymbol{v}^{(1)}$ vanish by construction (as they must for a perfect slip surface), we find that the $\boldsymbol{v}^{(1)}$ solution generates unbalanced interfacial stresses

$$S_\alpha^{(L)} = -k_\perp^2(2\mu + \lambda)u_\alpha^{(L1)} \quad (8)$$
$$S_\alpha^{(T)} = -k_\perp^2\mu u_\alpha^{(T1)}. \quad (9)$$

We now apply counter stresses to the interface to cancel these unbalanced stresses due to the perfect slip solution $\boldsymbol{v}^{(1)}$. Those counter stresses generate the fluid velocity correction $\boldsymbol{v}^{(2)}$ in the subphase due to the surface

rheology of the interface – specifically how it differs from that of a perfect slip interface assumed in the calculation of $\boldsymbol{v}^{(1)}$. One may calculate $\boldsymbol{v}^{(2)}$ induced by these counter stresses using the appropriate longitudinal and transverse Green's functions derived previously in Ref. [17]:

$$v_\alpha^{(L2)} = -i\omega \int S_\alpha^{(L)} \frac{(1+k_\perp z)\, e^{i\boldsymbol{k}_\perp\cdot\boldsymbol{x}_\perp + k_\perp z}}{(2\mu+\lambda)k_\perp^2 - 2i\omega\eta k_\perp} \frac{\mathrm{d}^2\boldsymbol{k}_\perp}{(2\pi)^2} \quad (10)$$

$$v_\alpha^{(T2)} = -i\omega \int S_\alpha^{(T)} \frac{e^{i\boldsymbol{k}_\perp\cdot\boldsymbol{x}_\perp + k_\perp z}}{\mu k_\perp^2 - i\omega\eta k_\perp} \frac{\mathrm{d}^2\boldsymbol{k}_\perp}{(2\pi)^2}, \quad (11)$$

where we have now returned to the real spatial domain.

Performing the integrals in Eqs. 10 and 11, we determine the velocity field correction $\boldsymbol{v}^{(2)}$ at the position of the tracer and use Faxén's law [22, 25] to find its contribution to the velocity of that particle. Adding the two contributions, we write the result using the susceptibility matrix χ_{ij} relating position U_i of the tracer to the applied force F_j

$$U_i = V_i/(-i\omega) = \chi_{ij} F_j. \quad (12)$$

Taking the limiting case of an incompressible monolayer, we find our main theoretical result. The in-plane part of the response function is given by

$$\frac{\chi_{xx}}{\chi^\infty} = 1 - \frac{9a}{16d} + \frac{a^3}{16d^3} - \frac{3a}{2\ell}\left[\mathrm{Ei}\left(\frac{-2d}{\ell}\right) - i\pi\right] e^{\left(\frac{2d}{\ell}\right)}, \quad (13)$$

with $\mathrm{Ei}(x)$ is the exponential integral function and $\chi^\infty = i/6\pi a\eta\omega$ the Stokes susceptibility of a spherical tracer infinitely far from interface. $\ell = \mu/(-i\eta\omega)$ is the Saffman-Delbrück (SD) length [27]. For a purely viscous monolayer, this length is simply the real ratio of membrane and subphase viscosities, but generally it is complex for viscoelastic monolayers. Its modulus sets the length scale over which in-plane monolayer momentum is transferred to the fluid subphase; it thus serves as a cut-off for the logarithmic divergence that appears in two-dimensional over-damped hydrodynamics [27].

At large distances from the interface, $d \gtrsim 10a$, the susceptibility approaches that given by the simple Stokes drag on a sphere for any SD length. Distant tracers are useless rheological probes. The key microrheological measurement involves studying how this susceptibility varies as the tracer's depth is decreased. For $\ell < a$ the particle response *increases* as the distance *decreases*, while for large SD lengths ($\ell > a$) the susceptibility *decreases* – see Fig. 2a,c. The quantity a/ℓ is qualitatively similar to a Knudsen number, or partial slip length [28], but the perfect slip limit is never reached here due to our enforcing surface incompressibility.

The phase of the complex SD length is determined by whether interfacial stresses are dissipative or reactive. In Fig. 2 we plot the response function for the two extreme cases of a purely elastic monolayer, where ℓ is imaginary, and the purely viscous one, where ℓ is real. As can be seen in Fig. 2a,c the imaginary part of the susceptibility does not vary much between the two extreme cases and is mainly dependent on the magnitude of the SD length. The real part, on the other hand, acquires a finite value when the surface is elastic but vanishes for purely viscous surface. Although we have assumed up to this point that the capillary number $Ca \ll 1$, it is straightforward to calculate the leading order effects of lowering the surface tension [23]. These surface height undulations at finite Ca have a subdominant effect on the tracer response for in-plane motion, but play a more important role in determining the spectrum of vertical fluctuations [23]. Details regarding the role of subdominant corrections to the susceptibility are included in the supplementary materials.

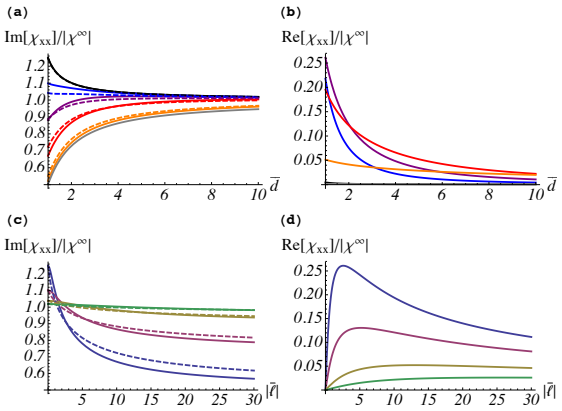

FIG. 2: The imaginary (a) and real (b) parts of the normalized tracer susceptibility χ for forces in the plane of the interface as a function of the tracer depth $\bar{d} = d/a$ for various values of the modulus of the SD length $|\ell|/a = 0, 1, 3, 10, 100, \infty$ (black, blue, purple, orange, gray). The phases are chosen to correspond to purely elastic (solid lines) and viscous (dashed lines) monolayers. The imaginary (c) and real (d) parts of χ as a function of $|\ell|/a$ for various depths below the monolayer: $\bar{d} = 1, 2, 5, 10$ (blue, purple, yellow, green). The imaginary part decreases as the surface modulus increases and the variation with $\bar{\ell}$ is greater for shallower depths.

We observe the fluctuation spectrum of tracers at various depths below monolayers of arachidic acid (AA), eicosanol, and dipalmitoylphosphatidylcholine (DPPC), for which previous studies demonstrate three different dependencies of viscosity on surface pressure [8–12, 29, 30]. AA is viscoelastic with a high elastic modulus in the frequency range studied: it should act as a rigid boundary and serve as a basic check on our data. Eicosanol has a phase transition to fluid phase above 15mN/m where the elastic modulus essentially vanishes and the viscosity decreases with increasing surface pressure. DPPC has a viscous, low-pressure phase that provides the best direct test of our technique as we can access surface pressures that range from the liquid condensed/liquid expanded (LC-LE) transition, for which an active measurement ex-

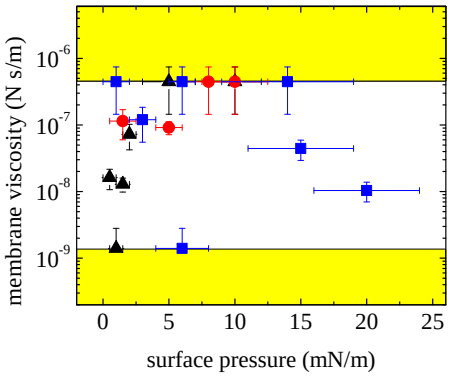

FIG. 3: Experimental results for tracer susceptibility converted to membrane viscosity for DPPC (black triangles), AA (red circles), and eicosanol (blue squares). The susceptibilities are converted to viscosities by the results shown in Fig. 2, for a tracer size $a = 5\mu m \pm 0.5\mu m$ and a depth of $d \sim a$. The yellow areas represent regions where the surface viscosities are inaccessible to the technique with the chosen experimental parameters – see text. The values of and observed variations in the surface viscosity are consistent with macroscopic measurements.

ists [11], and follow the viscosity measurements from this point to extremely low surface pressures for which the viscosity decreases by a factor of $\sim 10^3$ [12].

The position detection scheme has been described elsewhere [31] in detail. In short, we trap the tracer at a given depth below the surface using laser tweezers and analyze the light scattered off the particle with a quadrant photodiode to measure its thermally driven position fluctuations. By observing the change in the 5μm radius tracer's fluctuations (in the plane parallel to the interface) as a function of depth below the surface in a frequency band of 100 Hz around $f = \omega/2\pi \sim 10^3$ Hz and using the fluctuation-dissipation theorem [32], we measure the imaginary part of the tracer's response function. The response function is measured at depths of $d/a \sim 1 - 100$. Observing over a range of tracer depths enhances the resolution of the measurement. Data taken at depths $d > 25a$ yield the Stokes result; these are used to normalize the response function at shallower depths. The imaginary part of the response function as a function of depth is then fit using Eq. 13 using $|\ell|$ as the only adjustable parameter. All three monolayers are assumed to be purely viscous, which makes ℓ real. Fluctuation data and more details about the data acquisition and analysis are presented in the supplemental materials. We show the results of our measurements for tracers submerged below AA (red circles), eicosanol (blue squares), and DPPC (black triangles) monolayers as a function of surface pressure in Fig. 3. The imaginary part of the tracer response function, normalized by the Stokes result, is converted into inferred surface viscosities using Eq. 13 (see supplementary materials for raw susceptibility data).

As explained more fully in the supplement (see Fig. S4), for a tracer of given size, at a particular depth, there are physical upper and lower bounds on the fluctuation spectrum, corresponding to being below a free or a rigid surface, respectively. These regions are mapped to viscosity limits using Eq. 13, shown in yellow in Fig. 3. Within these regions the measurement technique is insensitive to the difference between the modulus and the limiting surface. By changing the frequency window and tracer size and depth, these limits can be moved to examine more or less compliant surfaces.

We observe the rheological signature of the structural phase transition of eicosanol at the expected surface pressure (15 mN/m), as reported in Ref. [9], with the expected decreasing viscosity with increasing surface pressure. Our surfaces viscosities are about one order of magnitude less than that previously measured macroscopically [9]. This smaller residual missing modulus may be due to frequency dependence of modulus (macroscopic measurements are performed at a few Hz while these were performed at 1kHz) [33], errors in the macroscopic measurements, or our assumption of a purely viscous response in the fluid phase when there may be a residual elastic component. In the future we will use active techniques designed to provide access to a wider frequency range to address this.

We find DPPC viscosities at higher pressures that are consistent with previous macroscopic measurements, indicating that the missing modulus from other microrheological techniques has been eliminated for this case. We observe a range of viscosities $(1 - 4) \times 10^{-7}$ Ns/m at surface pressures between (2 – 5) mN/m. Previous active rheology measurements (using a driven rotating disk) gave 4×10^{-7} Ns/m [11] at similar pressures and temperatures, where the monolayer was in the same phase. Our measurements were obtained in a higher frequency window than in previous results, but we expect the viscosity to be frequency independent in this lower pressure regime. Our results are also consistent with the upper bound of 10^{-6}Ns/m provided by macroscopic approaches [29]. We observe the continuous decrease of the measured viscosity with decreasing surface pressure over almost three orders of magnitude. Our viscosity measurement at lowest pressure is consistent with the single upper bound of 10^{-9} Ns/m for such very low pressure DPPC [12]. The ability to track the decreasing viscosity over this range demonstrates the large dynamic range of the microrheological technique.

Non-contact particle microrheology exploits a purely hydrodynamic coupling between the tracer and the monolayer. At the expense of this weaker coupling, one avoids issues associated with understanding the complex interaction of the probe and the monolayer. We have shown that this weaker coupling is sufficient to obtain

rheological data in this purely non-contact mode and to measure the viscosity of very low surface viscosity systems. In the future, we expect to study systems with complex viscoelastic responses, and to explore using the submerged tracer in a lateral scanning mode to detect spatial variations in surface rheology in heterogeneous monolayers and membranes. We also note that these results show that intracellular microrheological data taken near viscous cell membranes have to be corrected for this proximity effect.

The authors acknowledge NSF DMR-0907212 for partial support. AJL and AAE also acknowledge NSF DMR-1006162.

[1] C. M. Knobler and R. C. Desai, Annu. Rev. Phys. Chem. **43**, 207 (1992).

[2] V. M. Kaganer, H. Möhwald, and P. Dutta, Rev. Mod. Phys. **71**, 779 (1999).

[3] T. Bickel, Phys. Rev. E **75**, 041403 (2007).

[4] G. M. Wang, R. Prabhakar, Y. X. Gao, and E. M. Sevick, J. Opt. **13**, 044009 (2011).

[5] L. Joly, C. Ybert, and L. Bocquet, Phys. Rev. Lett. **96**, 046101 (2006).

[6] G. M. Wang, R. Prabhakar, and E. M. Sevick, Phys. Rev. Lett. **103**, 248303 (2009).

[7] K. E. Kasza, A. C. Rowat, J. Liu, T. E. Angelini, C. P. Brangwynne, G. H. Koenderink, and D. A. Weitz, Curr. Opin. Cell Biol. **19**, 101 (2007).

[8] R. S. Ghaskadvi, J. B. Ketterson, and P. Dutta, Langmuir **13**, 5137 (1997).

[9] C. F. Brooks, G. G. Fuller, C. W. Frank, and C. R. Robertson, Langmuir **15**, 2450 (1999).

[10] S. Q. Choi, S. Steltenkamp, J. A. Zasadzinski, and T. M. Squires, Nat. Commun. **2**, 312+ (2011).

[11] K. Kim, S. Q. Choi, J. A. Zasadzinski, and T. M. Squires, Soft Matter **7**, 7782 (2011).

[12] M. Sickert, F. Rondelez, and H. A. Stone, Europhys. Lett. **79**, 66005+ (2007).

[13] V. Prasad, S. A. Koehler, and E. R. Weeks, Phys. Rev. Lett. **97**, 176001+ (2006).

[14] V. Prasad and E. R. Weeks, Phys. Rev. Lett. **102**, 178302+ (2009).

[15] F. Ortega, H. Ritácco, and R. G. Rubio, Curr. Opin. Colloid Interface Sci. **15**, 237 (2010).

[16] T. M. Squires and T. G. Mason, Ann. Rev. Fluid Mech. **42**, 413 (2010).

[17] A. J. Levine and F. C. MacKintosh, Phys. Rev. E **66**, 061606 (2002).

[18] D. T. Chen, E. R. Weeks, J. C. Crocker, M. F. Islam, R. Verma, J. Gruber, A. J. Levine, T. C. Lubensky, and A. G. Yodh, Phys. Rev. Lett. **90**, 108301 (2003).

[19] J. C. Crocker, M. T. Valentine, E. R. Weeks, T. Gisler, P. D. Kaplan, A. G. Yodh, and D. A. Weitz, Phys. Rev. Lett. **85**, 888 (2000).

[20] A. J. Levine and T. C. Lubensky, Phys. Rev. Lett. **85**, 1774 (2000).

[21] D. Bonn, J. Eggers, J. Indekeu, J. Meunier, and E. Rolley, Rev. Mod. Phys. **81**, 739 (2009).

[22] J. Happel and H. Brenner, *Low Reynolds number hydrodynamics: with specific applications to particulate media* (Kluwer Boston, 1983).

[23] R. Shlomovitz, T. Boatwright, M. Dennin, and A. Levine, to be published (2012).

[24] L. D. Landau and E. M. Lifshitz, *Theory of elasticity* (Pergamon Press, Oxford, 1986), 3rd ed.

[25] S. Kim and S. J. Karrila, *Microhydrodynamics: Principles and selected applications* (Dover Publications, 2005).

[26] C. Pozrikidis, *Boundary Integral and Singularity Methods for Linearized Viscous Flow* (Cambridge University Press, Cambridge, UK, 1992).

[27] P. G. Saffman and M. Delbrück, Proc. Natl. Acad. Sci. **72**, 3111 (1975).

[28] E. Lauga and T. Squires, Phys. Fluids **17**, 103102 (2005).

[29] J. Krägel, J. B. Li, R. Miller, M. Bree, G. Kretzschmar, and H. Möhwald, Colloid Polym. Sci. **274**, 1183 (1996).

[30] R. S. Ghaskadvi, S. Carr, and M. Dennin, J. Chem. Phys. **111**, 3675 (1999).

[31] T. Boatwright, R. Shlomovitz, M. Dennin, and A. J. Levine, Phys. Fluids (2012).

[32] P. M. Chaikin and T. C. Lubensky, *Principles of condensed matter physics* (Cambridge University Press, 1995).

[33] M. Twardos and M. Dennin, Langmuir **19**, 3542 (2003).